Design and Simulation of a Frequency-Diverse Aperture for Imaging of Human-Scale Targets

OKAN YURDUSEVEN[1], (Member, IEEE), JONAH N. GOLLUB[1], (Member, IEEE), ALEC ROSE[2], DANIEL L. MARKS[1], AND DAVID R. SMITH[1], (Member, IEEE)

[1]Center for Metamaterials and Integrated Plasmonics, Department of Electrical and Computer Engineering, Duke University, Durham, NC 27708, USA
[2]Evolv Technologies, Inc., Waltham, MA 02451, USA

Corresponding author: O. Yurduseven (okanyurduseven@ieee.org)

ABSTRACT We present the design and simulation of a frequency-diverse aperture for imaging of human-size targets at microwave wavelengths. Predominantly relying on a frequency sweep to produce diverse radiation patterns, the frequency-diverse aperture provides a path to all-electronic operation, sampling a scene without the requirement for mechanical scanning or expensive active components. Similar to other computational imaging schemes, the frequency diverse aperture removes many hardware constraints by placing an increased burden on processing and analysis. While proof-of-concept simulations of scaled-down versions of the frequency-diverse imager and simple targets can be performed with relative ease, the end-to-end modeling of a full-size aperture capable of fully resolving human-size targets presents many challenges, particularly if parametric studies need to be performed during a design or optimization phase. Here, we show that an in-house developed simulation code can be adapted and parallelized for the rapid design and optimization of a full-size, frequency-diverse aperture. Using files of human models in stereolithography format, the software can model the entire imaging scenario in seconds, including mode generation and propagation, scattering from the human model, and measured backscatter. We illustrate the performance of several frequency-diverse aperture designs using images of human-scale targets reconstructed with various algorithms and compare with a conventional synthetic aperture radar approach. We demonstrate the potential of one aperture for threat object detection in security-screening applications.

INDEX TERMS Frequency-diversity, computational imaging, microwave imaging, microwaves, aperture, simulation.

I. INTRODUCTION

The use of microwaves and millimeter-waves for imaging has been the subject of considerable research, driven by the significant advantages associated with these schemes. In particular, radiation in the radio frequency (RF) bands is non-ionizing and thus ideally suited for a variety of imaging applications, including security-screening [1]–[5], through-wall imaging [6], [7], and biomedical imaging [8], [9].

To date, the two most widely studied imaging systems leveraging the RF bands are variants of synthetic aperture radar (SAR) and phased arrays. In the case of conventional SAR, a scene is sampled by measurements acquired from a transceiver that is physically moved over an area that forms a synthetic aperture [10]–[16]. Phased arrays and electronically scanned antenna systems, by contrast, populate an aperture with a dense array of antennas, each fed by a module containing a phase shifter and other active components; by controlling the amplitude and phase of the wavefront at every point on the aperture, these systems can perform imaging by synthesizing arbitrarily directed beams with electronic control [17]–[20]. Although good image fidelity has been achieved using SAR or phased array systems, the performance or accessibility of these systems can be limited in many contexts due to such factors as imaging speed or system complexity/cost.

To circumvent some of the limitations associated with traditional hardware and imaging modalities, modern imaging systems increasingly rely on computational imaging approaches that generalize the underlying concept of measurement to enable unusual and more flexible apertures. Systems that leverage computational imaging significantly reduce constraints on the RF system hardware, shifting more of the burden onto reconstruction algorithms and processing [21]–[29]. One such computational imaging platform, based
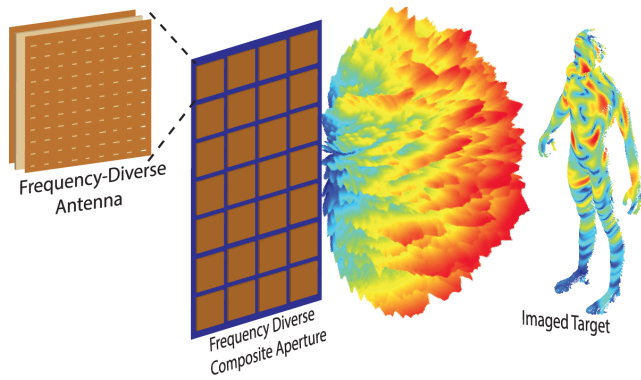
FIGURE 1. Imaging a human-scale target using the frequency-diversity scheme. The inset to the left depicts a simplified version of the parallel-plate cELC metasurface antenna. To the right, each unique field pattern is projected onto the target.

on a frequency-diverse antenna, has been shown to be a viable alternative to address some of the challenges associated with conventional systems [30]–[40]. The frequency-diverse antenna produces a set of radiation patterns as a function of the driving frequency, each of which has a complex and distinct spatial pattern throughout the scene volume. As the frequency is swept, a set of transmit antennas illuminate the scene, with a set of receive antennas collecting the reflected signal from the scene. The scene information is thus collected into measurements taken at a set of frequency points within the operating frequency band. Using computational imaging techniques, the set of measurements can be used to reconstruct an estimate of the scene. In Fig. 1 we depict imaging of a human-scale target with a frequency diverse aperture. As shown in Fig. 1, the synthesized composite aperture consists of an array of frequency-diverse antennas, producing complex radiation patterns illuminating the target. The antenna radiated fields exhibit strong variation as a function of frequency and are used to encode the scene information.

A number of proof-of-concept frequency-diverse imaging demonstrations at microwave frequencies have been recently presented, based on a metasurface antenna architecture [31]–[40]. The particular metasurface antenna used in [32]–[36] consisted of a parallel-plate waveguide structure with an array of subwavelength, complementary electric (cELC) metamaterial elements (or irises) etched into the upper conductor. The cELC elements act as resonant irises, with resonance frequencies governed by their particular geometry. The cELCs populated the entire upper conductor of the waveguide, laid out in a dense grid, each with a resonance frequency chosen randomly from within the operating frequency band. As the frequency is swept, only those cELCs whose resonance frequency corresponds to the driving frequency couple to the waveguide mode and radiate into the scene space; off-resonance cELCs radiate poorly, mostly resembling a conducting patch. Since at a given frequency only a random subset of the cELCs radiate, the corresponding radiation pattern is very irregular, with a relatively random set of lobes and nulls that vary as a function of frequency.

Given that the novelty and advantage of a frequency diverse imaging system are tied to the unconventional aperture, aperture design becomes the dominant task in the system development. A modeling platform must therefore be able to capture the essential features of the aperture architecture, allowing for performance optimization over certain key parameters. As with any aperture, diffraction and frequency bandwidth limit the amount of information that can be retrieved from a scene, which in turn implies a minimum number of independent measurements that must be obtained from a finite-size aperture to achieve diffraction-limited resolution. For the frequency-diverse metasurface antennas considered here, maximizing the number of measurement modes translates to optimizing the quality (Q-) factor of the antennas as well as maximizing coverage over spatial frequencies (k-space). These two parameters thus play an important role in the analyses and tradeoff studies presented here. The quality (Q-) factor for a metasurface antenna is determined both by the resistive and dielectric losses associated with the waveguide feed, as well as the radiative losses associated with the irises. The Q-factor of the antenna governs the number of distinct radiated fields (or the measurement modes) produced by the antenna over a given frequency bandwidth. It is thus desirable to maximize the Q-factor, minimizing the overlap between the frequency-indexed field patterns sampling the scene.

While a large Q-factor implies a potentially large number of modes, it does not guarantee that these modes will be orthogonal. A means of improving the independence of the measurement modes is to vary both the number and arrangement of irises over the antenna such that coverage in the spatial Fourier domain (k-space) is maximized. A detailed analysis shows that the k-space coverage between any two radiated field patterns can be related to the convolution of their patterns in the k-space; thus, part of an optimization process consists of analyzing the antenna parameters to maximize the k-space coverage [30], [31]. While the cELC-based metasurface antenna used in [32]–[36] proved the concept of frequency-diverse imaging, the low Q-factor and poor k-space coverage associated with this initial design limited the number of distinct radiative modes available from a frequency sweep. As an alternative approach, cavity-backed metasurface antennas were subsequently developed, in which a set of simple, non-resonant irises were used in place of the cELCs [31], [37]–[40]. The cavity-backed antennas replace the parallel plate waveguide feed with a closed cavity, achieved by terminating the open edges of the parallel-plate waveguide with conducting walls. With the larger field diversity achieved inside the cavity, and the higher radiative Q-factor due to the non-resonant irises, the cavity-backed antenna considerably improves both the measurement mode number and the mode diversity.

In prior work, we have introduced a simulation platform developed in the Matlab environment, which we refer to here as the *Virtualizer* [34], to investigate the performance of frequency-diverse apertures. This software platform is capable of simulating the details of the feed structure and radiative

properties of the antenna, as well as reflection from arbitrary reflectivity profiles that constitute a scene. In addition, the software can simulate the receive signal backscattered from the scene, and subsequently apply various reconstruction algorithms on the set of measurements to quantify expected imaging performance. Results obtained using the Virtualizer have been shown to be in good agreement with physical implementations, for smaller overall systems [38].

In terms of overall system design, the antenna design represents only the first step. It is often the case that the large aperture is formed by either introducing multiple feed points into a large aperture, or by tiling the overall aperture area with a collection of antennas. Thus, not only must the antenna parameters be determined—such as the Q-factor or k-space coverage—but system aspects must also be optimized, including the number of antennas; the size of the overall aperture; the placement of the antennas within the overall aperture (system layout); and ratio between the number of transmit and receive antennas. This level of design becomes a challenging task for large apertures designed for imaging human-size targets. Even with simulated and characterized antennas, investigating and optimizing the overall aperture experimentally is not feasible. Therefore, a fully functional simulation platform must be able to simulate not only the underlying frequency-diverse antennas, but also collections of antennas assembled into large overall apertures and large scenes. The simulation component is of particular importance in computational imaging schemes that rely on an accurately known forward model for both system calibration [40] and image reconstruction. Full-scale simulations must therefore be performed efficiently and quickly.

In this paper, we demonstrate the design and optimization of a full-scale frequency-diverse computational imaging system capable of resolving human-size objects. The Virtualizer software is applied to investigate the performance of apertures operating in the K-band frequency regime (17.5-26.5 GHz). In contrast to previous studies, the computational resources required for this effort are considerable, requiring parallelization of the code on graphics processing units (GPUs). Our goal here is to illustrate the level of design possible for large apertures, and demonstrate some of the basic properties of the frequency-diverse architecture with respect to human-size target imaging. This paper is organized as follows: In Section II we summarize the basic aspects of computational imaging and explain the concept of frequency-diverse imaging and image reconstruction. In Section III, we study the fundamental system aspects to synthesize a full-size frequency diverse aperture using the Virtualizer. Section IV demonstrates the implementation of the synthesized aperture for threat-object imaging in security-screening applications. Finally, Section V provides concluding remarks.

II. FREQUENCY-DIVERSE IMAGING AND IMAGE RECONSTRUCTION

The frequency-diverse imaging scheme involves encoding the scene information onto a set of measurements indexed by frequency, using pairs of antennas that produce frequency-dependent, complex radiation patterns. The radiated fields scatter from the reflectivity distribution in the scene; multiple scattering is ignored (first Born approximation) and the reflectivity at every point is assumed to be real and isotropic. Within the first Born approximation, the set of measurements are related to the scene reflectivity values by a *forward model* of the form:

$$\mathbf{g}_{i,j}(f) = \int_V \mathbf{E}_i^{Tx}(\mathbf{r}, f)\mathbf{E}_j^{Rx}(\mathbf{r}, f)\mathbf{f}(\mathbf{r})dV + n \qquad (1)$$

In (1), $\mathbf{g}$ is the signal collected from the scene over the operating frequency band and n represents a noise term. $\mathbf{E}_i^{Tx}$ denotes the fields radiated by the ith transmit antenna while $\mathbf{E}_j^{Rx}$ denotes the fields radiated by the jth receive antenna, both of which are propagated to the scene (at position $\mathbf{r}$ and frequency f) using the dyadic Green's functions [33], [34]. Applying (1) to a discrete number of voxels in the scene results in a matrix equation, with the combination of the fields from the transmit and receive antennas at those discrete locations forming the *measurement matrix,* given as $\mathbf{H} \propto \mathbf{E}^{Tx}\mathbf{E}^{Rx}$. Therefore, it is evident that the measurement matrix, $\mathbf{H}$, within the imaging integral in (1) includes the radiation pattern information of the antennas. If the measurement matrix is known, then (1) can be used to reconstruct an estimate of the scene reflectivity (or contrast) vector, $\mathbf{f}$, which poses an inverse problem. Given that we use M measurement modes to reconstruct a scene consisting of N three-dimensional (3D) voxels, (1) can be expressed as follows:

$$\mathbf{g}_{Mx1} = \mathbf{H}_{MxN}\mathbf{f}_{Nx1} + \mathbf{n} \qquad (2)$$

Reconstructing the scene in (2), $\mathbf{f}_{Nx1}$, requires that the measurement matrix $\mathbf{H}$ be inverted. However, in general, $M \neq N$ and therefore $\mathbf{H}$ does not possess an inverse. Instead, we can apply approximate reconstruction techniques, such as matched filter and least-squares [36] to obtain an estimate of the scene reflectivity, $\mathbf{f}_{est}$. The matched filter approach can be considered the most basic reconstruction algorithm, as it involves taking the Hermitian transpose (conjugate-transpose) of the measurement matrix $\mathbf{H}$, with just a single matrix multiplication required to reconstruct an estimate of the scene, $\mathbf{f}_{est} = \mathbf{H}^\dagger\mathbf{g}$. Unlike the matched filter algorithm, the least-squares reconstruction is an iterative technique, taking the matched filter reconstruction as an initial estimate of the scene to converge to a better solution by means of a non-linear iterative process. The least-squares algorithm minimizes the objective function $\arg \min \|\mathbf{g} - \mathbf{Hf}\|_2^2$.

For an imaging problem on the scale of human-size targets, the scene size can be significant, requiring a very large number of discretization voxels, N. Examining (2), it can be seen that increasing N increases the size of $\mathbf{H}$. An imaging problem producing a large $\mathbf{H}$ poses two major challenges. First, calculation and further processing of $\mathbf{H}$ can consume a significant amount of time; and second, the

amount of memory required to store the elements of **H** can be prohibitively large. It is therefore desirable to minimize the size of **H** in (2). One way of achieving this reduction is to reduce the number of discretization voxels, N, by using a constraint on the reconstruction volume. For example, instead of reconstructing a full rectangular volume enclosing a human-size target, the reconstruction volume boundaries can be reduced to a constrained and conformal region determined by the surface of the target. In an actual implementation of a computational imaging system, a structured light illuminator can be used to locate the target and determine the region of space to voxelize. Commercial sensors that operate at infrared wavelengths, such as the Microsoft Kinect sensor, can potentially be used for this purpose. We refer here to the reduced reconstruction volume as the *region of interest* (ROI). We mimic the effect of a structured light sensor within the Virtualizer code by applying a padding to the surface of a human-size target, as illustrated in Fig. 2.
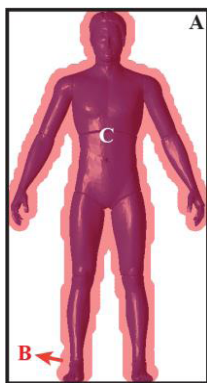

FIGURE 2. Regions for imaging (A) full volume enclosing the target; (B) constrained ROI; (C) imaged human-size object.

Fig. 2 illustrates a typical reduction of the target ROI for reconstruction of the RF image, assuming the surface of the target can be determined using an IR or optical sensor. Without applying the constraint, the ROI is defined by the rectangular volume enclosing the human-size object (A in Fig. 2). Once the surface constraint is applied, the ROI is reduced to a volume determined by the surface of the object with a padding factor (B in Fig. 2). It should be noted that, in the context of security imaging, the padding factor should be selected large enough to ensure that any threat objects placed on the human body remain inside the defined constrained region.

Although the use of surface constraints significantly reduces N, for the imaging problem discussed in this work, calculating the measurement matrix **H** is still a challenging task. As will be explained in the next section in detail, discretizing the constrained scene at the resolution limit of the synthesized full-size aperture considered in this work results in $N = 122,082$ voxels. If we assume that the system supports $M \approx 200,000$ measurement modes, the total amount of memory required for **H** (when calculated using single precision) is larger than 90 GB. This memory

problem is often circumscribed by finding a translation-invariant form or approximation to (1), at which point both simulation and inversion can be carried out via fast Fourier Transforms (FFTs). However, this is not always possible for the general class of multi-offset apertures operating in the radiative near-field. Instead, we employ the partitioning scheme introduced in [41], which does not rely on translation invariance, but instead uses a multi-scale approach similar to the multilevel fast multi-pole method [42]. In essence, the method consists of three steps. First, the scene is divided into subdomains, and both transmitter and receiver fields are propagated to each subdomain. Second, the fields are divided by a spherical wave phase approximation such that the remainder can be assumed slowly varying within each subdomain. Third, the remainders are interpolated onto the fine grid, and the phase term is then restored. More details can be found in [41], but for the purpose of this paper, utilizing only two levels, it was shown that this method can approach $O(N^{(3/2)})$, compared to $O(N^2)$ for the brute force method and $O(N\log(N))$ for FFT-based methods. This gain in speed was sufficient for the human-size modelling shown, while retaining the needed generality to investigate the unusual class of aperture presented. Moreover, it should also be noted that given the storage and processing requirements for the imaging problem discussed in this work, the use of the partitioning approach was important in that it made the calculations computationally feasible due to the reduced memory requirements.

III. MULTI-STATIC FREQUENCY-DIVERSE SYSTEM MODELING FOR IMAGING OF FULL-SIZE HUMAN TARGETS

The tradeoff between the Q-factor and radiation efficiency sets a general limit on the number of modes available from a single frequency-diverse antenna. Additional measurement modes can be obtained by increasing the number of antennas within the composite aperture, leading to a multi-static aperture defined by a number of frequency-diverse antennas. A feasible imaging system thus consists of an array of transmit and receive antennas with a single source that can be sequentially switched to the various transmit antennas. Multistatic operation has the advantage of increasing angular diversity, as the scene can be viewed from multiple angles for different transmit and receive antenna pairs [43]. The efficacy of any particular aperture configuration can be understood within the context of k-space. Because it is desirable to obtain the most information from the fewest measurements possible, the measurement modes should generally minimize the degree of redundancy between any two measurement modes. One means of reducing the number of measurements is to ensure that the measurement modes cover as many spatial frequencies (Fourier space) as possible (k-space support), with minimal overlap. As will be shown later, the coverage in k-space associated with a transmit and receive antenna pair can be determined by the convolution of the fields radiated by the antennas in k-space [30]. Achieving angular and

frequency-diverse operation is important in that it enables different subsets of the k-space to be sampled, extending the k-space support. It also ensures that for any given transmit and receive antenna pair, the sampling redundancy in k-space is minimized, increasing the information content collected from the scene as a function of frequency.

Within the context of frequency-diverse imaging, using multiple transmit and receive antennas also increases the total number of measurement modes, M. The total number of measurement modes supported by a frequency-diverse, multistatic imaging system is equal to the *number of transmit antennas × number of receive antennas × number of frequency points*. Comparing M to N, it is evident that there are three possible conditions for a computational imaging system: over-sampled ($M > N$); equally-sampled ($M = N$); and under-sampled ($M < N$). This observation holds under the condition that the measurement modes are perfectly orthogonal (no correlation between the modes exists) and the scene is discretized at the diffraction limit. However, in reality, the modes exhibit correlation to a certain degree (albeit minimized); therefore, increasing M to reconstruct a scene consisting of N voxels might be desired; however, one needs to consider the size of **H** as a limiting factor. As given in (2), increasing M also increases the size of **H**, and thus the size of the data set that must be processed and stored.

To place the frequency-diverse imaging system into context, we first investigate what might be considered a best-case scenario in terms of the orthogonality of the measurement modes. SAR consists of a set of measurements that are essentially orthogonal in k-space and provide maximal coverage of k-space for a given aperture. This orthogonality implies that the information received from the scene at each spatial sampling point is nearly independent from the subsequent sampling points (minimized information redundancy). However, it should be emphasized that although excellent image fidelity can be obtained using the SAR technique, data acquisition time required for SAR can be significant if the antennas are mechanically scanned.

A conventional SAR system can be readily modeled within the Virtualizer framework. As shown in Fig. 3, to achieve SAR imaging, we define a single, low-gain antenna and assume it is physically positioned at points along a raster scan over a 2 m × 2 m synthesized aperture. The scene consists of a full-size human model, imported as a file in stereolithography (STL) format, and positioned at a distance of $d = 1.2$ m from the aperture. After importing the STL file, a collection of 3D voxels is built encompassing the region of the model, with each voxel assigned a reflectivity of $\Gamma = 0.8$ to approximate the reflectivity of human skin at microwave frequencies [43] ($\Gamma = 0$ denotes a voxel that is non-reflective while $\Gamma = 1$ is fully-reflective). An additional padding region, conformal to the model, is also voxelized to ensure all features are captured in the reconstruction. Since voxels within the volume of the model would not be accessible in an actual experiment, interior voxels are ultimately removed from the reconstruction region.
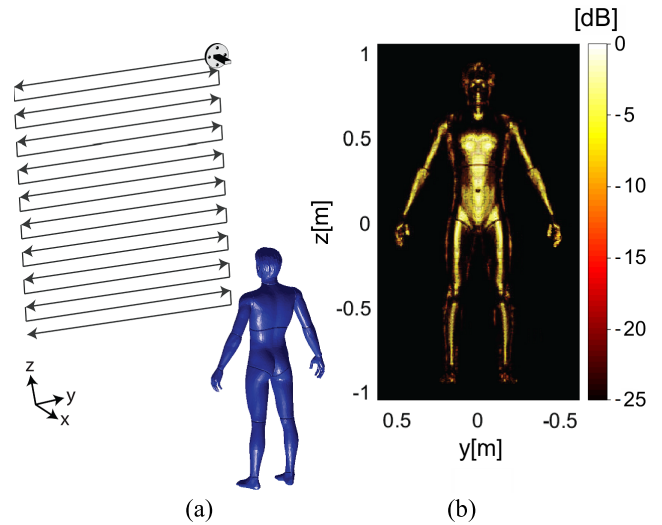

FIGURE 3. Imaging of a human-size target using conventional monostatic SAR scheme (a) SAR imaging (b) matched-filter reconstructed image.

The bandwidth for the simulated SAR system is taken from 17.5 GHz to 26.5 GHz (K-band), with the scene sampled at the midband Nyquist limit. The matched filter algorithm is applied for image reconstruction. The simulations presented here were performed using a computer with an Intel Core i7 CPU, 128 GB RAM and NVidia Titan X GPU. The imaging parameters for the SAR scenario are provided in Table 1.

TABLE 1. System parameters for SAR imaging.

Aperture Size	2 m x 2 m
Sampling Interval	7 mm
Spatial Sampling Points	334 x 334
Frequency Band	K-band (17.5 – 26.5 GHz)
Measurement Modes (M)	163,592
Extent of the Imaged Human Target	26 cm (x-axis) 1 m (y-axis) 1.9 m (z-axis)
Distance	1.2 m
Scene Discretization Voxel Size	1.5 cm (range) 5 mm (cross-range)
Number of Voxels (N)	872,336 (full volume) 122,082 (constrained ROI)

The initial step of the simulation procedure, assuming the properties of the sub-aperture antennas have been computed, is to discretize the region of interest (ROI) into a set of voxels of dimensions consistent with the resolution limit of the synthesized aperture. Using the SAR resolution equations [3], [36], the range and cross-range resolution limits corresponding to the specific aperture can be calculated as 1.6 cm and 6.5 mm, respectively. Thus, the constrained ROI is discretized into cubic voxels of size 1.5 cm (range) and 5 mm (cross-range), resulting in $N = 122,082$ voxels. From Table 1, it can be seen that the unconstrained volume consists of $N = 872,336$ voxels, suggesting that constraining the ROI reduces the number of voxels (and therefore the size of

the measurement matrix **H**) by a factor of 86%. The padding factor for the constrained ROI is chosen to be 5 cm.

Although the simulated SAR scheme in Fig. 3(a) is monostatic, as will be shown later, the Virtualizer can easily be extended to simulate multistatic configurations. As can be seen in Fig. 3(b), the SAR image reveals a clear outline of the imaged human model. The simulation time for the considered SAR scenario was calculated to be ≈4 hours. This long computation time is required to simulate raster scanning of the probe antenna at each sampling point on the aperture plane. For each sampling, the fields from the probe antenna are propagated to the scene, a process repeated by the total number of spatial sampling points, 334 × 334 as given in Table 1. The field propagation at each sampling point was run on the GPU. Due to the parallelized multicore architecture, calculation of the fields using the GPU can be performed in a fast manner. However, for the demonstrated SAR scenario, we are limited by the time required to access the GPU memory at each sampling point. We note that the simulation time for the demonstrated SAR scenario can be optimized by using Fourier-based methods relying on FFT algorithms [3], [44], which can readily be implemented in the Virtualizer. The purpose of the SAR imaging scenario simulated here is to provide a comparison for the image reconstruction quality, not to compare reconstruction times.

As described above, there are many paths to the design of a frequency-diverse, metasurface antenna. We first present an analysis of the imaging properties of a metasurface antenna formed using resonant, cELC elements, similar to antennas previously demonstrated in smaller scale studies [32]–[36]. The parallel-plate waveguide metasurface antenna consists of a dielectric substrate with complementary electric (cELC) elements etched into the upper conductor. A depiction of the parallel-plate metasurface antenna structure is shown in Fig. 4.
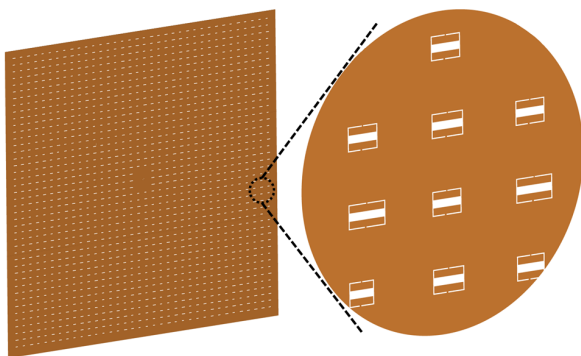

FIGURE 4. Depiction of the cELC metasurface antenna structure.

Each cELC exhibits a Lorentzian resonance response for its effective magnetic polarizability, with the resonance frequency related to the specific geometry of the resonator. As shown in the detail portion of Fig. 4, certain geometrical features within each cELC element (such as its length) are chosen randomly from a defined range of parameters, such

that the resonance frequency of each cELC element has a random value that varies over the operational bandwidth—in this case selected to be the K-band (17.5 – 26.5 GHz). Only a subset of cELC elements will radiate at any given frequency, such that a frequency sweep will produce a set of frequency-dependent radiation patterns (or measurement modes) interrogating the scene.

For imaging of human-size objects, an important parameter to be decided is the dimension of the overall aperture that will be tiled by a number of antennas. For this analysis, we assume the same synthesized composite aperture dimensions that we used for the SAR analysis in Fig. 3: 2 m × 2 m. Given that the size of the composite aperture is fixed, the number of the antennas that can be fit within the area covered by the aperture is limited by the size of the antennas. In this work, the dimensions of each of the metasurface antennas filling the aperture are chosen to be 10 cm × 10 cm [31].

With the sizes of the composite aperture and the antennas filling the aperture selected, the effect of the Q-factor of the constituent aperture antennas must be evaluated. To isolate the impact of the antenna Q-factor on imaging performance, we first consider a small imaging system in the Virtualizer, consisting of eight transmit and eight receive frequency-diverse antennas of the type shown in Fig. 4 imaging a gun phantom. The imaging configuration is shown in Fig. 5. In this simulation, we vary the Q-factor of the antennas and compare the reconstructed images of the gun phantom as a function of Q-factor. The system parameters for this simulation are given in Table 2.
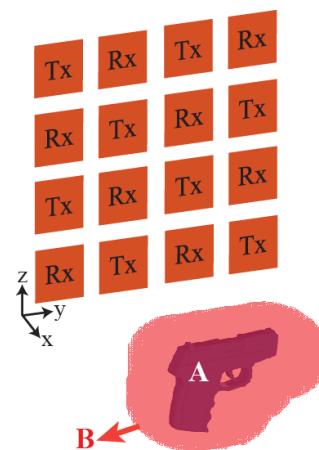

FIGURE 5. Imaging of a gun phantom using a small-system. (A) imaged gun phantom (B) constrained ROI. Tx and Rx denote the transmit and receive antennas, respectively.

For the reconstructed images shown in Fig. 6, we make use of the matched filter reconstruction algorithm with the reconstruction time measured to be 0.03 seconds. The ROI (region B in Fig. 5) consists of the phantom, with an additional padding region that includes the space up to 5 cm from the surface of the phantom. The constrained ROI consists of $N = 7,919$ voxels, reduced by a factor of 89.1% in

TABLE 2. System parameters for the small system imaging a gun phantom.

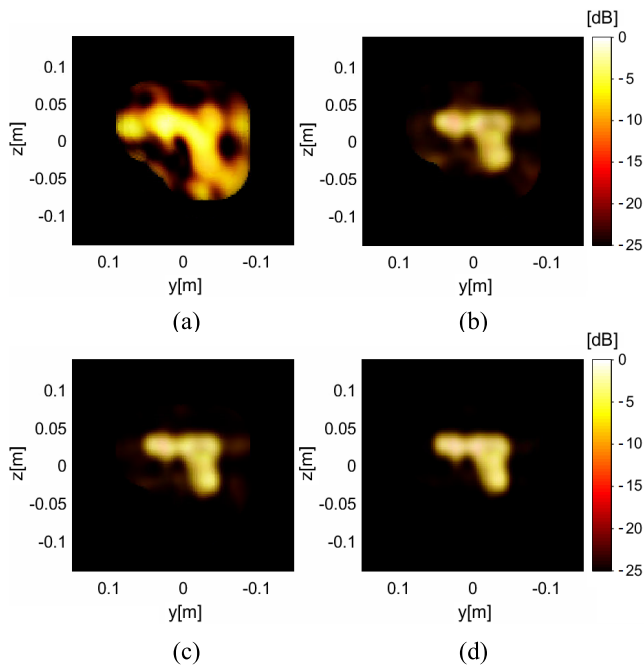| Aperture Size	0.6 m x 0.6 m
Frequency Band	K-band (17.5 – 26.5 GHz)
Number of Frequency Points	100
Measurement Modes (M)	6,400
Size of Gun Phantom	10 cm x 8 cm
Distance	1.2 m
Scene Discretization Voxel Size	1 cm (range) 5 mm (cross-range)
Number of Voxels (N)	73,017 (full volume) 7,919 (constrained ROI)

FIGURE 6. Reconstructed images of the gun phantom as a function of antenna Q-factor (a) $Q = 10$ (b) $Q = 100$ (c) $Q = 250$ (d) $Q = 500$.

comparison to the number of voxels within the full (non-constrained) volume, $N = 73,017$. As can be seen in Fig. 6, the reconstructed image of the gun phantom improves as the Q-factor of the antennas is increased. The image reconstructed using antennas with $Q = 10$ in Fig. 6(a) exhibits considerably high side-lobes. Increasing the Q-factor to $Q = 100$ in Fig. 6(b), the actual outline of the gun phantom becomes evident with the side-lobes significantly reduced. Increasing the Q-factor to $Q = 250$ in Fig. 6(c) and $Q = 500$ in Fig. 6(d), the side-lobes are further suppressed. All subsequent simulations are performed with antennas having a Q-factor of $Q = 500$. Although larger Q-factors correspond to an increased mode number, in reality, there is an inverse relationship between the Q-factor and the radiation efficiency of a frequency-diverse antenna [30]. Therefore, it might not be feasible to achieve an experimental Q-factor of $Q = 500$ in actual applications. Using the Virtualizer, we can model a

frequency-diverse antenna with any desired Q-factor. In this work, we make the assumption that $Q = 500$ is an upper-bound limit and physically realizable.

Any physically realizable system will have noise from various sources added to the signal. The signal to noise ratio (SNR) of an imaging system will be directly impacted by the radiation efficiency of the antennas sampling the scene; therefore, the optimization of the Q-factor represents a trade-off between mode number and radiation efficiency. Based on systems presented in previous work [38], the studies presented here assume a 20 dB SNR level introduced into the Virtualizer. The noise was added to the signal collected from the scene, **g** in (2), and exhibits a Gaussian distribution.

To achieve the full-size aperture needed for imaging of human-size targets, a number of the sub-aperture antennas must be used to fill the aperture area. While increasing the number of antennas increases the total number of measurement modes, M, increasing the number antennas also necessarily increases the dimension of the **H**-matrix, and the amount of data needed for processing. It is therefore necessary to find the optimum number of antennas, trading off image quality for processing speed. The actual optimum number will depend on many factors, including the desired resolution of the images and the available processing hardware. To illustrate the tradeoff, we fix the size of the composite aperture to 2 m × 2 m, and vary the number of the antennas, as shown in Fig. 7. For each configuration, a human-size target is imaged. Similar to the SAR scenario considered in Fig. 3, the padding factor for the constrained ROI is chosen to be 5 cm and the ROI is discretized into cubic voxels in accordance with the range and cross-range resolution limits of the synthesized composite aperture, resulting in $N = 122,082$ voxels (constrained ROI). For the distribution pattern of the antennas within the overall aperture, we make use of a random grid as depicted in the system layout shown in Fig. 7. The system parameters for the simulations are given in Table 3.
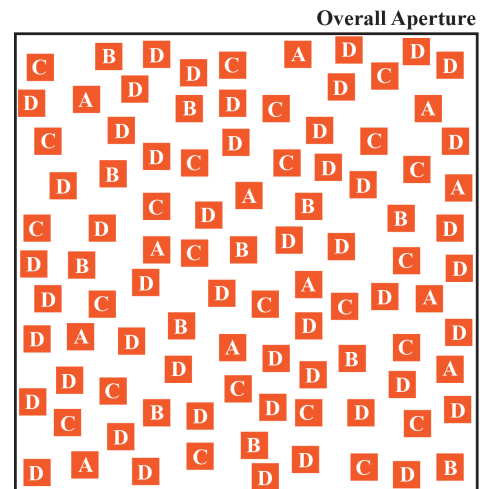

FIGURE 7. Synthesized overall aperture (2 m × 2 m) with varying number of antennas (sparsity) filling the aperture.

TABLE 3. System parameters for the full-size frequency-diverse aperture with cELC metasurface antennas imaging a human-size target.

Aperture Size	2 m x 2 m
Frequency Band	K-band (17.5 – 26.5 GHz)
Number of Frequency Points	100
Extent of the Imaged Human Target	26 cm (x-axis) 1 m (y-axis) 1.9 m (z-axis)
Distance	1.2 m
Scene Discretization Voxel Size	1 cm (range) 5 mm (cross-range)
Number of Voxels (N)	872,336 (full volume) 122,082 (constrained ROI)

The total number of measurement modes for the configurations shown in Fig. 7 are given in Table 4. It should be noted that for the configurations reported in Table 4, the number of the transmit and receive antennas is equal.

TABLE 4. Number of measurement modes for different sparsity configurations.

Configuration	Number of Antennas (Total)	Number of Measurement Modes (M)
A	12	3,600
A+B	24	14,400
A+B+C	48	57,600
A+B+C+D	96	230,400

Investigating Table 4, it can be seen that the upper-bound limit for the number of antennas filling the composite aperture was selected to be 96, modelling a system that is developed and under consideration and will be reported elsewhere [45]. For experimental imaging, a direction we are currently working on, one might consider cross-coupling between the antennas a challenge. However, the antenna cross-coupling can easily be removed as part of a background subtraction.

The reconstructed images of the human-size target are presented in Fig. 8. For image reconstruction the matched filter technique was used.

From Fig. 8(a), it is evident that the image reconstructed using the 12-antenna configuration (configuration A) does not provide useful information. This can be attributed to two factors. First, for this configuration the scene is heavily under-sampled, $M < N$, and $M = 3,600$ measurements is not enough to capture the information content of the scene consisting of $N = 122,082$ voxels to have a meaningful reconstruction. Second, using only 12 antennas results in a poor sampling of the k-space. We next increase the number of antennas within the synthesized aperture from 12 to 24 (configuration A+B), bringing the number of measurement modes to $M = 14,400$. Although slightly improved, as shown in Fig. 8(b), the reconstructed image using the 24-antenna configuration exhibits similar response to the 12-antenna configuration and the system is still heavily
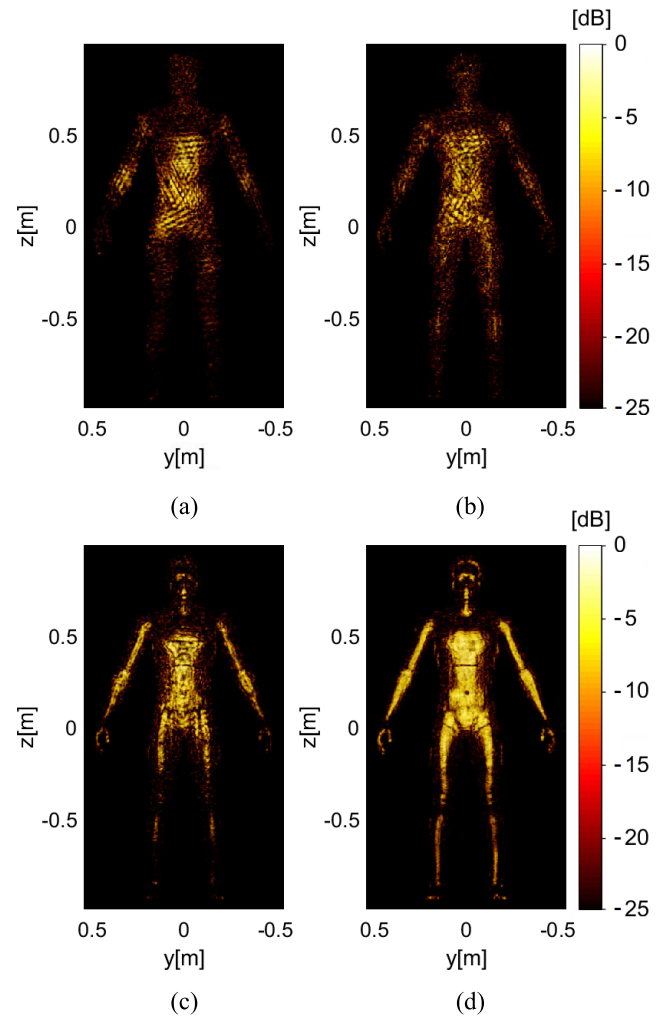
FIGURE 8. Matched filter reconstructed images of the human size target as a function of sparsity of the antennas filling the aperture (a) 12-antenna (b) 24-antenna (c) 48-antenna (d) 96-antenna.

under-sampled. Increasing the number of the antennas to 48 (configuration A+B+C) results in the system producing $M = 57,600$ measurement modes. As shown in Fig. 8(c), the image of the human target reconstructed using the 48-antenna configuration exhibits far better quality. Finally, we increase the number of antennas from 48 to 96 (configuration A+B+C+D), bringing the number of measurement modes to $M = 230,040$. Different from the previous configurations, the 96-antenna configuration is over-sampled, $M > N$. The image of the human-size target reconstructed using the 96-antenna configuration in Fig. 8(d) exhibits much higher fidelity, limited only by the specularity of the target; that is, certain reflections from the target are simply not captured with the available aperture.

The images presented in Fig. 8 were reconstructed using the matched filter algorithm. As mentioned earlier, matched filter reconstruction is a linear operation and does not involve an iterative process. Using iterative approaches, such as least-squares reconstruction, better image estimates can be obtained at the expense of increasing the image
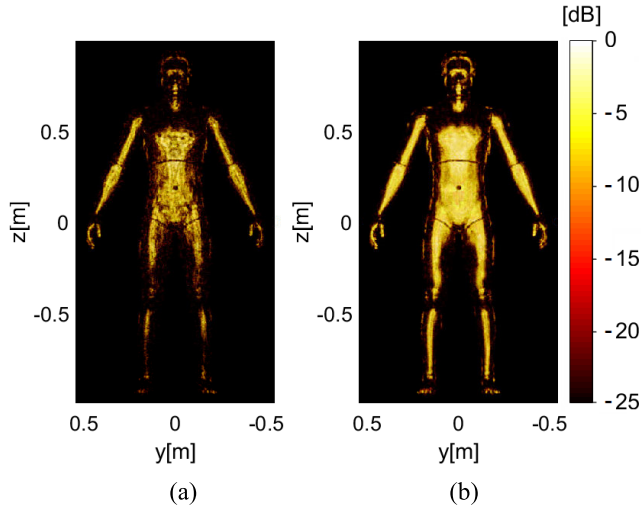
FIGURE 9. Least-squares images of the human-size target reconstructed using (a) 48-antenna (b) 96-antenna configurations.

reconstruction time. In Fig. 9, the least-squares images of the human shaped object reconstructed using the 48-antenna and 96-antenna configurations are demonstrated. For least-squares reconstruction, Tikhonov regularization was used, improving the conditioning of the inverse problem by truncating the singular values below a certain threshold [46]–[48]. Comparing the reconstructed images in Figs. 8 and 9, it is evident that the images reconstructed using the least-squares algorithm are of better quality.

The simulation process in the Virtualizer can be grouped into three stages; a) partitioning the scene and calculation of the fields, b) forward model, and c) image reconstruction. The calculation time for the first stage (scene partitioning and field calculation) is 1.06 minutes (12-antenna configuration), 1.59 minutes (24-antenna configuration), 3.27 minutes (48-antenna configuration), and 9.52 minutes (96-antenna configuration). Similar to the first stage, as the number of antennas is increased, the simulation time for the forward model (second stage) increases. Here, we particularly focus on two configurations, 48-antenna and 96-antenna, providing meaningful reconstructions of the human-size target as shown in Figs. 8 and 9. The forward model stage requires 7.03 seconds for the 48-antenna configuration and 18.3 seconds for the 96-antenna configuration. Using the matched-filter algorithm, the image reconstruction (third stage) time was measured to be 2.44 seconds for the 48-antenna configuration and 4.14 seconds for the 96-antenna configuration. Using the least-squares algorithm, the reconstruction time was reported to be 22.6 seconds and 53.7 seconds, respectively. It should be noted here that for a selected ROI, the first stage (scene partitioning and field calculation) needs to be performed only once. Therefore, if a sufficiently large ROI is selected, this step can be pre-calculated, leaving only the forward model and image reconstruction to be performed when the scene is changed.

Another important factor for designing a frequency-diverse imaging system is the ratio between the number of the transmit and receive antennas. For the aperture configurations studied above, the number of the transmit and receive antennas was selected to be equal; for example, the 96-antenna configuration consists of 48 transmit and 48 receive antennas. However, for practical applications, this assumption does not necessarily hold. For most practical applications, this choice depends on the number of the transmit and receive channels supported by the signal source of the system. We can investigate the impact of changing the transmit/receive antenna ratio on the image quality. For this study, we consider the composite aperture consisting of 96 antennas in total and vary the transmit/receive antenna ratio as given in Table 5.

TABLE 5. Varying number of transmit and receive antennas filling the synthesized aperture.

Layout	Number of Tx Antennas	Number of Rx Antennas	Tx/Rx Ratio	Number of Modes
I	12	84	1/7	100,800
II	84	12	7	100,800
III	48	48	1	230,400

As can be seen in Table 5, in comparison to configurations I and II, the number of measurement modes supported by configuration III is higher. The reconstructed images of the human-size target obtained using the configurations given in Table 5 are shown in Fig. 10. Due to the shorter amount of time required for image reconstruction, the matched filter technique was used for this analysis.

Investigating Fig. 10, it can be seen that the images reconstructed using configurations I and II are noisier in comparison to the image of the human-size target reconstructed using configuration III. This is expected since, as shown in Table 5, configuration III exhibits more measurement modes, $M = 230,400$ in comparison to configurations I and II, providing only $M = 100,800$ measurement modes.

For the studies shown up to this point, we have used parallel-plate waveguide cELC metasurface antennas. To demonstrate the versatility of the Virtualizer software, we replace the waveguide metasurface antenna by a Mills-Cross metasurface antenna, previously proposed in [31]. The modeling of the parallel-plate metasurface waveguide antenna in the Virtualizer is realized by approximating the aperture as a collection of radiating magnetic dipoles [33], [34]. This analytical approximation provides the basis for an extremely good assessment of the behavior of an imaging system, but does not enable direct prediction of the fields or measurement modes associated with an actual device. In particular, coupling between the radiating elements can shift the resonances of the elements, or even modify the driving waveguide mode, such that exact analytical predictions are not possible. However, the Virtualizer software can nevertheless be used to create accurate predictions of imaging performance by importing the fields measured near the aperture plane of an antenna by means of a near-field scan. These fields can be back-propagated to the aperture surface, and converted into
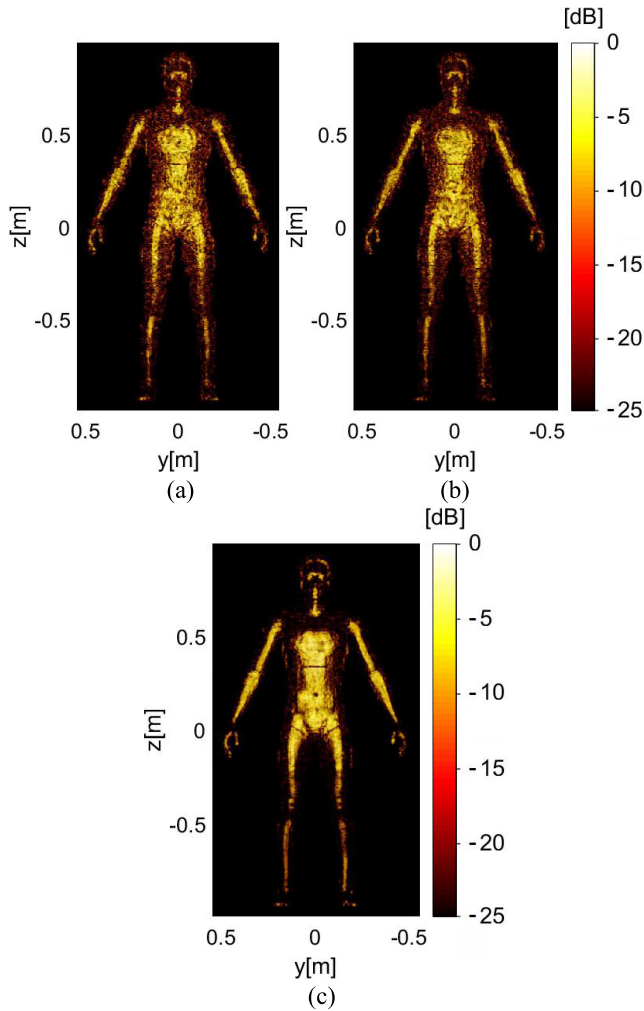
FIGURE 10. Matched filter images of the human-size target reconstructed using different configurations exhibiting varying transmit/receive antenna ratios (a) Tx/Rx ratio = 1/7 – configuration I (b) Tx/Rx ratio = 7 – configuration II (c) Tx/Rx ratio = 1 – configuration III.

FIGURE 11. Mills-Cross cavity antennas (a) receive antenna (b) transmit antenna (c) depiction of the receive antenna (d) depiction of the transmit antenna.

a set of equivalent dipoles; once this step is done, all other aspects of the simulation can be applied without further modification. To demonstrate the technique, we fabricated two Mills-Cross cavity antennas, transmit and receive, with the radiating irises etched onto the front surface of the antennas forming a Mills-Cross pattern as shown in Fig. 11. Note that the irregular cavity walls, formed by a via fence in the actual samples, create a generally irregular field distribution for the driving waveguide modes. Because of the diversity in the waveguide mode, only simple irises are needed to form the metasurface. The number of irises is also reduced to maximize the Q-factor. The Mills-Cross panels exhibit a Q-factor of $Q = 330$.

We measure the electric fields radiated by the antennas using a planar near-field scanner, NSI200 V-3×3, and import the fields into the Virtualizer. Within the Virtualizer, we then synthesize a full-aperture—configuration A+B+C+D shown in Fig. 7—using the Mills-Cross antennas. For this analysis, the number of the transmit and receive antennas was selected to be equal, 48 transmit and 48 receive, producing
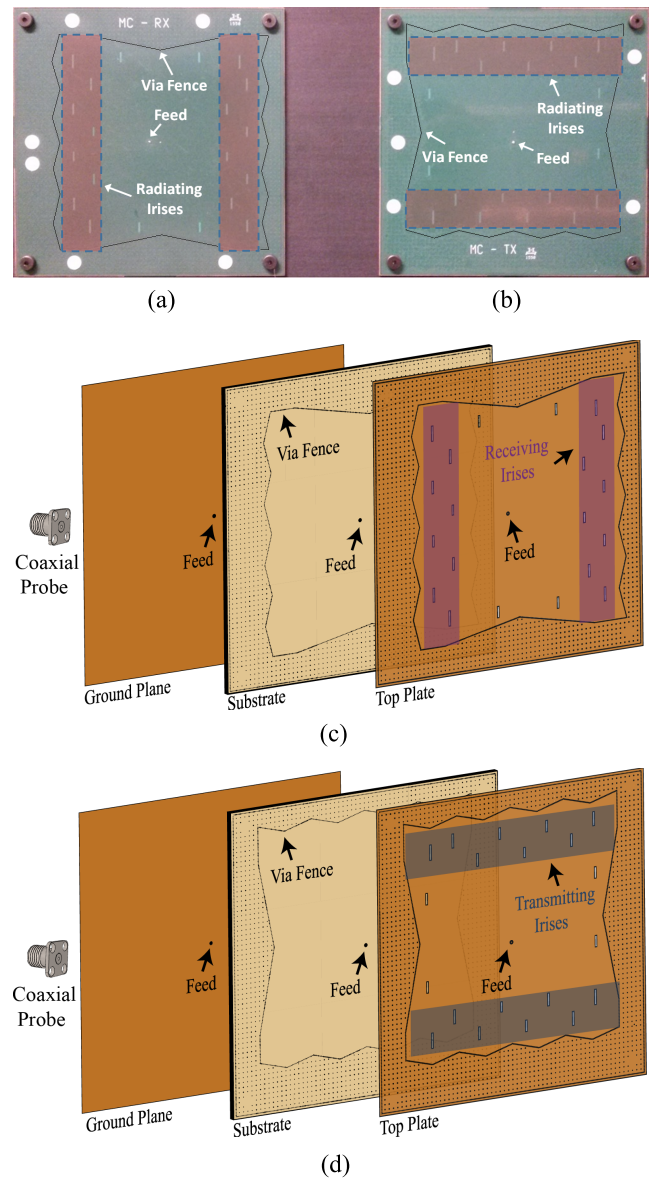
$M = 230,400$ measurement modes. The system parameters for this simulation are given in Table 6.

The matched-filter and least-squares reconstructed images of the human-size target are shown in Fig. 12. As shown in Fig. 12, both reconstructed images reveal a clear outline of the target with the least-squares reconstructed image exhibiting better quality.

IV. K-SPACE, MODE ORTHOGONALITY AND SINGULAR VALUE DECOMPOSITION ANALYSES

We can use the Virtualizer to perform k-space analyses of different aperture configurations. For a frequency-diverse aperture, it is desired that the modes generated by the antennas sample the Fourier components in the k-space with a minimum redundancy. Sampling the non-overlapping

TABLE 6. System parameters for the full-size frequency-diverse aperture with Mills-Cross metasurface antennas imaging a human-size target.

Aperture Size	2 m x 2 m
Frequency Band	K-band (17.5 – 26.5 GHz)
Number of Frequency Points	100
Number of Measurements (*M*)	230,400
Extent of the Imaged Human Target	26 cm (x-axis) 1 m (y-axis) 1.9 m (z-axis)
Distance	1.2 m
Scene Discretization Voxel Size	1 cm (range) 5 mm (cross-range)
Number of Voxels (*N*)	872,336 (full volume) 122,082 (constrained ROI)

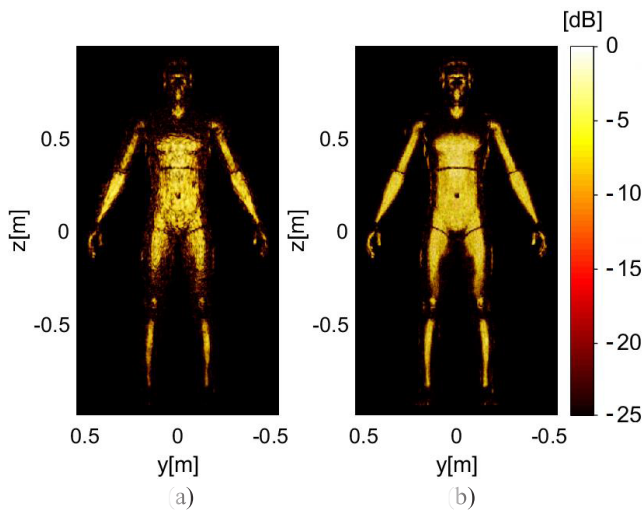**FIGURE 12.** Reconstructed images of the human-sized target using the Mills-Cross antennas (a) matched-filter (b) least-squares.

FIGURE 13. Investigated sub-volume enclosing part of the human-scale target for k-space analysis.

We first investigate the k-space coverage of the synthesized aperture considered in Fig. 7 as a function of varying the number of transmit and receive antennas filling the aperture. For this analysis, we use the cELC metasurface antennas and calculate the k-space patterns for the 12-antenna (configuration A) and 96-antenna (configuration A+B+C+D) layouts. The obtained k-space patterns are shown in Fig. 14.

sections of the k-space maximizes the information content of the modes encoding the scene information. The achievable imaging resolution is governed by the filling of the k-space (k-space support). In order to analyze the overall k-space support of the full-system, we choose a small domain of the size of $10\lambda \times 10\lambda \times 10\lambda$ (λ calculated at 17.5 GHz), enclosing a sub-section of the imaged human-scale target as shown in Fig. 13.

The fields radiated by the transmit and receive antennas are then propagated to the investigated sub-domain using the 3D Green's function propagator; $\mathbf{E}_{vol}^{Tx}(\mathbf{r}, f)$ and $\mathbf{E}_{vol}^{Rx}(\mathbf{r}, f)$, respectively, and Fourier transformed into the spectral domain, $\mathcal{F}\{\mathbf{E}_{vol}^{Tx}(\mathbf{r}, f)\}$ and $\mathcal{F}\{\mathbf{E}_{vol}^{Rx}(\mathbf{r}, f)\}$. Here, the points in the subdomain are denoted by $\mathbf{r}$ while the Fourier transform is done for all frequency points (as a function of f) across the K-band. The overall k-space coverage can be given as the superposed convolution of the Fourier transformed fields swept through all possible transmit and receive antennas across the K-band. The resolution of the overall system can be determined by taking the inverse Fourier transform of the k-space pattern, suggesting that a wider k-space support results in a finer imaging resolution.
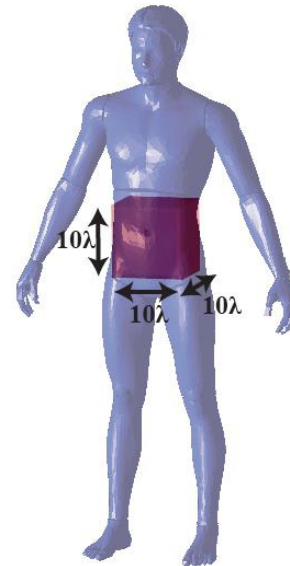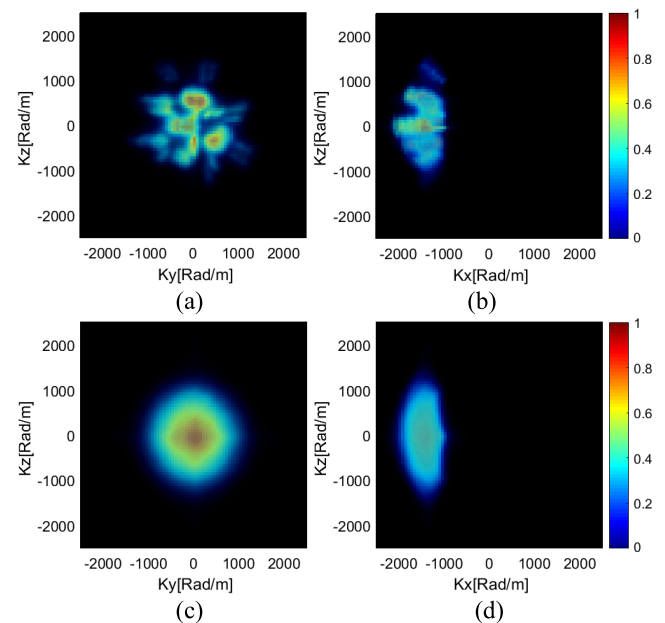

FIGURE 14. K-space patterns as a function of the number of the antennas filling the synthesized aperture; 12-antenna configuration (a) Ky-Kz plane (b) Kx-Kz plane; 96-antenna configuration (c) Ky-Kz plane (d) Kx-Kz plane.

Investigating Fig. 14, it can be seen that increasing the number of antennas filling the composite aperture improves the k-space support. For the analysis shown in Fig. 14, we

varied only the number of antennas while the Q-factor of the antennas remained the same, $Q = 500$. Next, we select the 96-antenna configuration and investigate the k-space pattern as a function of the Q-factor (and therefore mode-diversity). For this study, we set the Q-factor of the antennas to $Q = 100$ and $Q = 500$, respectively, and investigate the obtained k-space patterns shown in Fig. 15. It is evident in Fig. 15 that a superior k-space pattern is obtained when increasing the Q-factor of the antennas.
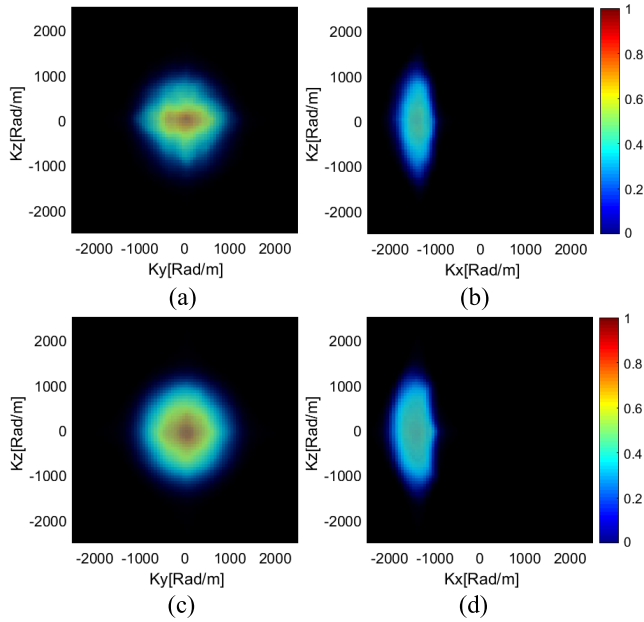

FIGURE 15. K-space patterns as a function of the Q-factor of the antennas; $Q = 100$ (a) Ky-Kz plane (b) Kx-Kz plane; $Q = 500$ (c) Ky-Kz plane (d) Kx-Kz plane.

Following the k-space analyses for the composite aperture synthesized using the cELC metasurface antennas, the 96-antenna configuration was synthesized using the Mills-Cross antennas to provide a comparison between the k-space patterns. In Figs. 16(a) and (b), the k-space patterns for the two composite apertures are shown. For this demonstration, we highlight two regions in the k-space patterns. The dashed blue circle represents the inner k-sphere calculated at 17.5 GHz with a radius of $r_1 = \frac{2w_1}{c}$, where w_1 is the angular frequency at 17.5 GHz. The solid red circle denotes the outer k-sphere exhibiting a radius of $r_2 = \frac{2w_2}{c}$, where w_2 is the angular frequency at 26.5 GHz. The 3D representation of the k-spheres is shown in Fig. 16(c). It should be noted that as the K-band is sampled at 100 frequency points, there are 100 possible k-spheres for this demonstration. However, for the sake of clarity, we show only the upper and lower-bound limits. The k-space patterns demonstrated in Figs. 16(a) and (b) are normalized with respect to the most redundantly sampled Fourier component. Analyzing Fig. 16, it can be seen that the aperture synthesized using the Mills-Cross antennas samples an increased number of Fourier components, resulting in widening the k-space support.
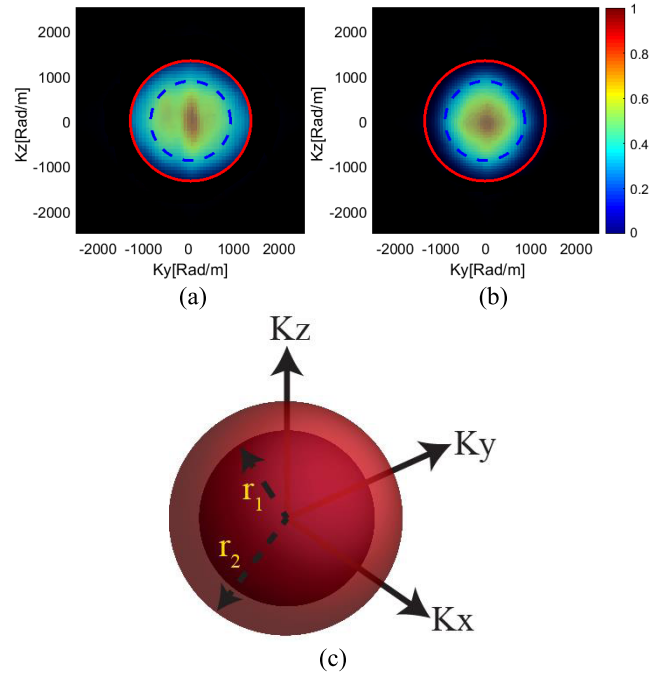

FIGURE 16. K-space analysis (a) composite aperture with Mills-Cross metasurface antennas (Ky-Kz plane) (b) composite aperture with cELC metasurface antennas (Ky-Kz plane) (c) depiction of 3D k-spheres – inner sphere (17.5 GHz) and outer sphere (26.5 GHz).

An important metric by which to assess the orthogonality of the measurement modes produced by a frequency diverse imaging system is the singular value spectrum of the measurement matrix **H** in (2). One path to assessing the effective information content in the collection of measurement modes can be achieved by means of a singular value decomposition (SVD) analysis of **H** in the Virtualizer. Reducing the correlation between the measurement modes results in a singular value spectrum that falls off slowly with increasing mode number, improving the conditioning of the **H** matrix [30], [31]. For this study, we analyze the singular value spectrum of the full-size aperture, consisting of 96 antennas distributed on a random grid as shown in Fig. 7 (configuration A+B+C+D). We first use the cELC metasurface antennas and investigate the singular value spectrum of the synthetized aperture as a function of varying the Q-factor. We then use the Mills-Cross antennas to synthesize the same aperture and perform the SVD analysis. As shown in Fig. 17(a), for the SVDs, we make use of a 2D scene with the surface area of the scene selected to be $A = 2m^2$, which is in accordance with the surface area of the human-size target imaged in this work. Discretizing the scene at the resolution limit results in $N = 41,209$. The calculated SVD patterns are shown in Fig. 17(b).

It can be seen in Fig. 17(b) that although all three configurations have $M = 230,400$ modes, the total number of significant singular values is limited to $N = 41,209$ as $N < M$ and N corresponds to the diffraction limit. It is evident in Fig. 17(b) that increasing the Q-factor of the antennas increases the orthogonality of the measurement
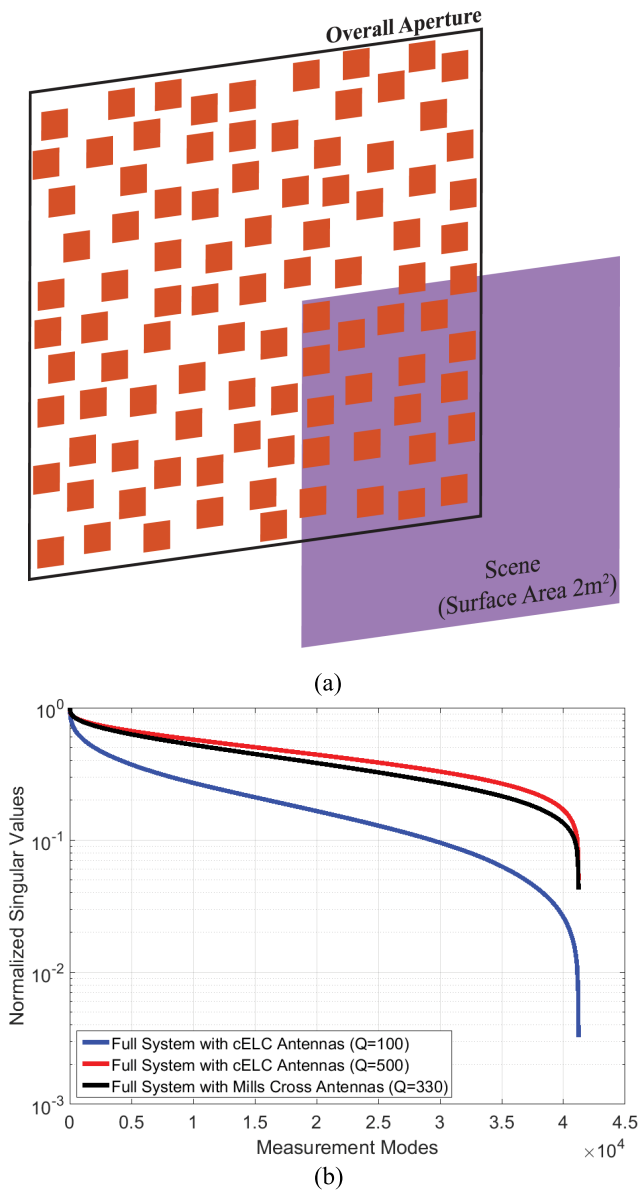
(a)

(b)

FIGURE 17. SVD analyses (a) system configuration (b) SVD patterns of the full-size aperture filled using different types of frequency-diverse antennas with varying Q-factors.

modes forming the **H**-matrix. A flat singular value spectrum suggests a minimized correlation between the measurement modes, increasing the information content provided by the modes at adjacent frequency points as the frequency is swept over the K-band.

V. THREAT OBJECT IMAGING AND RANGE COLOR CODING

In this work, using the synthesized frequency-diverse composite aperture, we reconstruct 3D images of the human-scale target. In view of this, we can further benefit from the depth information by color-coding the reconstructed images—a feature potentially relevant in security-screening applications. In view of this, we consider the full-system layout in

Fig. 7 using the parallel-plate metasurface antennas depicted in Fig. 4, and image a human-size target with a gun phantom attached to the body, as shown in Fig. 18.
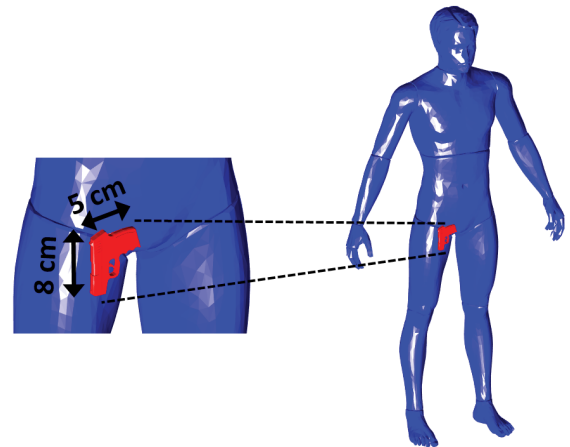

FIGURE 18. Human-size target with a gun phantom (5 cm×8 cm) attached to the body.

A significant challenge in security-screening applications is the identification of the threat objects (often metal) from the human body. Similar to metals, human skin is a good reflector within the microwave and millimeter-wave frequency bands [43]. Therefore, the discrimination of the threat objects from the human body can be a difficult task, based on two-dimensional sections. This difficulty can clearly be seen in the reconstructed images shown in Fig. 19. For the images demonstrated in Fig. 19, the reflectivity values for the human-size target and the gun phantom were selected to be $\Gamma = 0.8$ and $\Gamma = 1$, respectively.
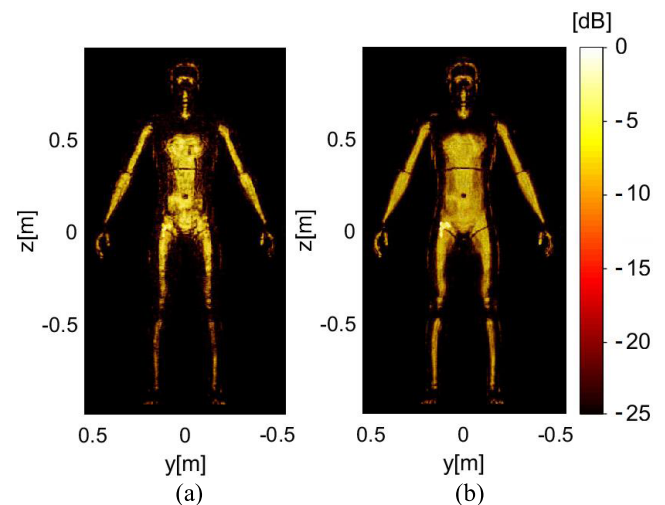

FIGURE 19. Reconstructed images of the human-size target with a gun phantom attached to the body as a threat object (a) matched-filter (b) least-squares.

By making use of the nearly tomographic nature of the data supplied in a coherent, RF imaging system, additional post-processing techniques can be implemented to improve

the contrast of threat objects on a person. The reconstructed images shown in Fig. 19 exhibit reflectivity-only information with the brighter regions representing a stronger reflection. However, since metals and human skin exhibit similar reflectivity response within the frequency band of interest in this work, K-band, the object mostly blends in with the human target. Since depth information is also available in the reconstructed image, we can apply depth color-coding along the range dimension. In this scheme, we use different colors to represent the reconstructed voxels as a function of their distance from the aperture. Due to the additional thickness introduced by the threat-objects, when depth color-coded, they appear in a different color from the color of the surface of the body onto which they are attached. The color-coded reconstructed images are shown in Fig. 20.
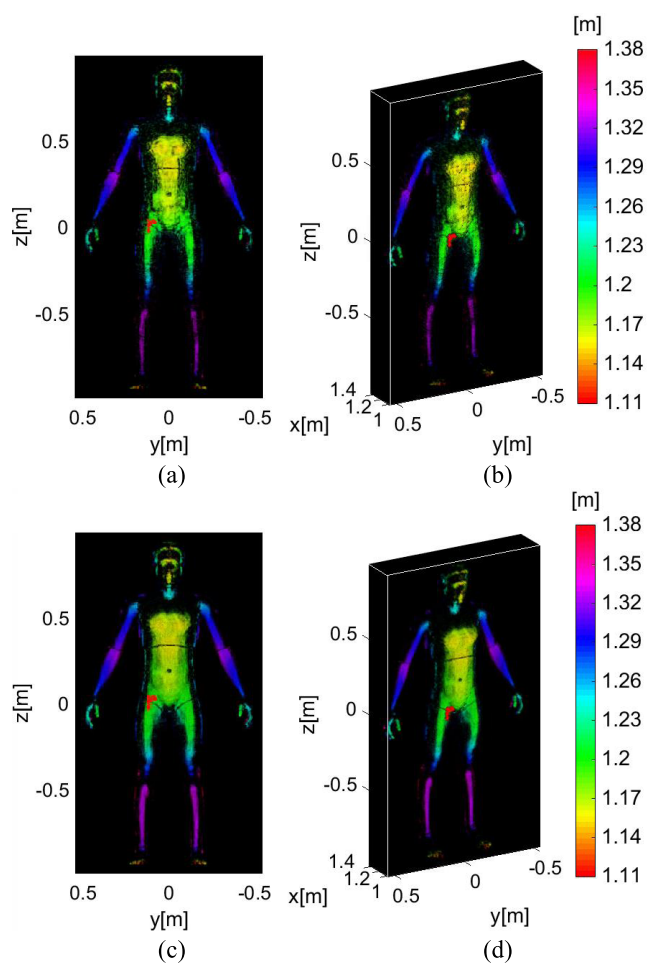

FIGURE 20. Color-coded reconstructed images of the human-size target with the gun phantom; matched filter (a) front-view (b) 3D perspective; least-squares (c) front-view (d) 3D perspective.

The outline of the gun phantom in the color-coded reconstructed images in Fig. 20 is evident. Comparing Figs. 19 and 20, it is clear that taking advantage of the nearly tomographic-like information contained in the reconstructions can be used to help identify foreign objects in security screening applications. The range color-coding performed

in Fig. 20, though far too simplistic to be a viable algorithm, nevertheless provides an indication of what might be possible when other aspects of the information are used.

VI. CONCLUSION

This paper has demonstrated the design of a full-size frequency-diverse aperture for imaging of human-size objects. Using the Virtualizer simulation tool, we have analyzed the effect of fundamental system aspects, such as Q-factor, antenna sparsity (number of antennas filling the synthesized aperture) and transmit / receive antenna ratio, on the reconstructed images and k-space response. In addition to the frequency-diverse aperture exhibiting a multistatic operation, we have also designed a SAR aperture performing imaging on a monostatic basis for comparison. Extending the developed concept to security-screening applications, we have shown the imaging of human-size targets with threat objects and implemented a color-coding scheme to facilitate the threat detection. We believe that the Virtualizer holds a significant potential for the design and optimization of imaging systems (monostatic, bistatic and multistatic) without the necessity to perform these studies experimentally, which can be costly and time-consuming. Although shown for the K-band frequency regime, the Virtualizer can readily be extended to millimeter-wave and THz band imaging applications.

REFERENCES

[1] D. M. Sheen, D. L. McMakin, and T. E. Hall, "Three-dimensional millimeter-wave imaging for concealed weapon detection," *IEEE Trans. Microw. Theory Techn.*, vol. 49, no. 9, pp. 1581–1592, Sep. 2001.

[2] S. Demirci, H. Cetinkaya, E. Yigit, C. Ozdemir, and A. A. Vertiy, "A study on millimeter-wave imaging of concealed objects: Application using back-projection algorithm," *Prog. Electromagn. Res.*, vol. 128, pp. 457–477, Jun. 2012.

[3] X. Zhuge and A. G. Yarovoy, "A sparse aperture MIMO-SAR-based UWB imaging system for concealed weapon detection," *IEEE Trans. Geosci. Remote Sens.*, vol. 49, no. 1, pp. 509–518, Jan. 2011.

[4] O. Yurduseven, "Indirect microwave holographic imaging of concealed ordnance for airport security imaging systems," *Prog. Electromagn. Res.*, vol. 146, pp. 7–13, Apr. 2014.

[5] J. A. Martinez-Lorenzo, F. Quivira, and C. M. Rappaport, "SAR imaging of suicide bombers wearing concealed explosive threats," *Prog. Electromagn. Res.*, vol. 125, pp. 255–272, Feb. 2012.

[6] Y. Wang and A. E. Fathy, "Advanced system level simulation platform for three-dimensional UWB through-wall imaging SAR using time-domain approach," *IEEE Trans. Geosci. Remote Sens.*, vol. 50, no. 5, pp. 1986–2000, May 2012.

[7] T. S. Ralston, G. L. Charvat, and J. E. Peabody, "Real-time through-wall imaging using an ultrawideband multiple-input multiple-output (MIMO) phased array radar system," in *Proc. IEEE Int. Symp. Phased Array Syst. Technol.*, Oct. 2010, pp. 551–558.

[8] N. K. Nikolova, "Microwave imaging for breast cancer," *IEEE Microw. Mag.*, vol. 12, no. 7, pp. 78–94, Dec. 2011.

[9] M. Elsdon, O. Yurduseven, and D. Smith, "Early stage breast cancer detection using indirect microwave holography," *Prog. Electromagn. Res.*, vol. 143, pp. 405–419, Nov. 2013.

[10] A. W. Doerry and F. M. Dickey, "Synthetic aperture radar," *Opt. Photon. News*, vol. 15, no. 11, pp. 28–33, 2004.

[11] A. Moreira, P. Prats-Iraola, M. Younis, G. Krieger, I. Hajnsek, and K. P. Papathanassiou, "A tutorial on synthetic aperture radar," *IEEE Geosci. Remote Sens. Mag.*, vol. 1, no. 1, pp. 6–43, Mar. 2013.

[12] M. Fallahpour, J. T. Case, M. T. Ghasr, and R. Zoughi, "Piecewise and Wiener filter-based SAR techniques for monostatic microwave imaging of layered structures," *IEEE Trans. Antennas Propag.*, vol. 62, no. 1, pp. 282–294, Jan. 2014.

[13] F. Qi, I. Ocket, D. Schreurs, and B. Nauwelaers, "A system-level simulator for indoor mmW SAR imaging and its applications," *Opt. Exp.*, vol. 20, no. 21, pp. 23811–23820, 2012.

[14] R. K. Amineh, J. McCombe, and N. K. Nikolova, "Microwave holographic imaging using the antenna phaseless radiation pattern," *IEEE Antennas Wireless Propag. Lett.*, vol. 11, pp. 1529–1532, 2012.

[15] J. Laviada, A. Arboleya-Arboleya, Y. Alvarez-Lopez, C. Garcia-Gonzalez, and F. Las-Heras, "Phaseless synthetic aperture radar with efficient sampling for broadband near-field imaging: Theory and validation," *IEEE Trans. Antennas Propag.*, vol. 63, no. 2, pp. 573–584, Feb. 2015.

[16] D. Smith, O. Yurduseven, B. Livingstone, and V. Schejbal, "Microwave imaging using indirect holographic techniques," *IEEE Antennas Propag. Mag.*, vol. 56, no. 1, pp. 104–117, Feb. 2014.

[17] B.-H. Ku *et al.*, "A 77–81-GHz 16-element phased-array receiver with ±50° beam scanning for advanced automotive radars," *IEEE Trans. Microw. Theory Techn.*, vol. 62, no. 11, pp. 2823–2832, Nov. 2014.

[18] S. Withington, G. Saklatvala, and M. P. Hobson, "Partially coherent analysis of imaging and interferometric phased arrays: Noise, correlations, and fluctuations," *J. Opt. Soc. Amer. A*, vol. 23, no. 6, pp. 1340–1348, 2006.

[19] G. L. Charvat, L. C. Kempel, E. J. Rothwell, C. M. Coleman, and E. L. Mokole, "An ultrawideband (UWB) switched-antenna-array radar imaging system," in *Proc. IEEE Int. Symp. Phased Array Syst. Technol.*, Oct. 2010, pp. 543–550.

[20] A. J. Fenn, D. H. Temme, W. P. Delaney, and W. E. Courtney, "The development of phased-array radar technology," *Lincoln Lab. J.*, vol. 12, no. 2, pp. 321–340, 2000.

[21] D. Shrekenhamer, C. M. Watts, and W. J. Padilla, "Terahertz single pixel imaging with an optically controlled dynamic spatial light modulator," *Opt. Exp.*, vol. 21, no. 10, pp. 12507–12518, 2013.

[22] D. J. Brady, K. Choi, D. L. Marks, R. Horisaki, and S. Lim, "Compressive holography," *Opt. Exp.*, vol. 17, no. 15, pp. 13040–13049, 2009.

[23] D. Shin, A. Kirmani, V. K. Goyal, and J. H. Shapiro, "Photon-efficient computational 3-D and reflectivity imaging with single-photon detectors," *IEEE Trans. Comput. Imag.*, vol. 1, no. 2, pp. 112–125, Jun. 2015.

[24] O. S. Cossairt, D. Miau, and S. K. Nayar, "Scaling law for computational imaging with spherical optics," *J. Opt. Soc. Amer. A*, vol. 28, no. 12, pp. 2540–2553, 2011.

[25] M. F. Duarte *et al.*, "Single-pixel imaging via compressive sampling," *IEEE Signal Process. Mag.*, vol. 25, no. 2, pp. 83–91, Mar. 2008.

[26] D. J. Brady, *Optical Imaging and Spectroscopy*. New York, NY, USA: Wiley, 2009.

[27] D.-H. Shin, C.-W. Tan, B.-G. Lee, J.-J. Lee, and E.-S. Kim, "Resolution-enhanced three-dimensional image reconstruction by use of smart pixel mapping in computational integral imaging," *Appl. Opt.*, vol. 47, no. 35, pp. 6656–6665, 2008.

[28] S. S. Welsh, M. P. Edgar, R. Bowman, P. Jonathan, B. Sun, and M. J. Padgett, "Fast full-color computational imaging with single-pixel detectors," *Opt. Exp.*, vol. 21, no. 20, pp. 23068–23074, 2013.

[29] J. A. Martinez-Lorenzo, J. H. Juesas, and W. Blackwell, "A single-transceiver compressive reflector antenna for high-sensing-capacity imaging," *IEEE Antennas Wireless Propag. Lett.*, vol. 15, pp. 968–971, 2016.

[30] D. L. Marks, J. Gollub, and D. R. Smith, "Spatially resolving antenna arrays using frequency diversity," *J. Opt. Soc. Amer. A*, vol. 33, no. 5, pp. 899–912, 2016.

[31] O. Yurduseven, J. N. Gollub, D. L. Marks, and D. R. Smith, "Frequency-diverse microwave imaging using planar mills-cross cavity apertures," *Opt. Exp.*, vol. 24, no. 8, pp. 8907–8925, 2016.

[32] J. Hunt *et al.*, "Metamaterial apertures for computational imaging," *Science*, vol. 339, no. 6117, pp. 310–313, 2012.

[33] G. Lipworth *et al.*, "Metamaterial apertures for coherent computational imaging on the physical layer," *J. Opt. Soc. Amer. A*, vol. 30, no. 8, pp. 1603–1612, 2013.

[34] G. Lipworth *et al.*, "Comprehensive simulation platform for a metamaterial imaging system," *Appl. Opt.*, vol. 54, no. 31, pp. 9343–9353, 2015.

[35] J. Hunt *et al.*, "Metamaterial microwave holographic imaging system," *J. Opt. Soc. Amer. A*, vol. 31, no. 10, pp. 2109–2119, 2014.

[36] O. Yurduseven *et al.*, "Resolution of the frequency diverse metamaterial aperture imager," *Prog. Electromagn. Res.*, vol. 150, pp. 97–107, Jan. 2015.

[37] T. Fromenteze *et al.*, "Computational imaging using a mode-mixing cavity at microwave frequencies," *Appl. Phys. Lett.*, vol. 106, no. 19, p. 194104, 2015.

[38] O. Yurduseven, V. R. Gowda, J. Gollub, and D. R. Smith, "Printed aperiodic cavity for computational and microwave imaging," *IEEE Microw. Wireless Compon. Lett.*, vol. 26, no. 5, pp. 367–369, May 2016.

[39] O. Yurduseven, V. R. Gowda, J. N. Gollub, and D. R. Smith, "Multistatic microwave imaging with arrays of planar cavities," *IET Microw., Antennas Propag.*, vol. 10, no. 11, pp. 1174–1181, Aug. 2016.

[40] O. Yurduseven, J. N. Gollub, K. P. Trofatter, D. L. Marks, A. Rose, and D. R. Smith, "Software calibration of a frequency-diverse, multistatic, computational imaging system," *IEEE Access*, vol. 4, pp. 2488–2497, 2016.

[41] A. Boag, "A fast multilevel domain decomposition algorithm for radar imaging," *IEEE Trans. Antennas Propag.*, vol. 49, no. 4, pp. 666–671, Apr. 2001.

[42] J. Song, C.-C. Lu, and W. C. Chew, "Multilevel fast multipole algorithm for electromagnetic scattering by large complex objects," *IEEE Trans. Antennas Propag.*, vol. 45, no. 10, pp. 1488–1493, Oct. 1997.

[43] S. S. Ahmed, *Electronic Microwave Imaging With Planar Multistatic Arrays*. Berlin, Germany: Logos Verlag Berlin GmbH, 2014.

[44] Y. Alvarez *et al.*, "Fourier-based imaging for multistatic radar systems," *IEEE Trans. Microw. Theory Techn.*, vol. 62, no. 8, pp. 1798–1810, Aug. 2014.

[45] J. N. Gollub *et al.*, "Large metasurface aperture for millimeter wave computational imaging at the human-scale," *Science*, submitted 2016.

[46] C. Liu, Y. Wang, and P. A. Heng, "A comparison of truncated total least squares with Tikhonov regularization in imaging by ultrasound inverse scattering," *Phys. Med. Biol.*, vol. 48, no. 15, pp. 2437–2451, Jul. 2003.

[47] C. W. Groetsch, *The Theory of Tikhonov Regularization for Fredholm Equations of the First Kind*. Boston, MA, USA: Pitman, 1984.

[48] L. Reichel, H. Sadok, and A. Shyshkov, "Greedy Tikhonov regularization for large linear ill-posed problems," *Int. J. Comput. Math.*, vol. 84, no. 8, pp. 1151–1166, 2007.

OKAN YURDUSEVEN (S'09–M'11) received the B.Sc. and M.Sc. degrees in electronics and communications engineering from Yildiz Technical University, Istanbul, Turkey, in 2009 and 2011, respectively, and the Ph.D. degree in electromagnetics from Northumbria University, Newcastle upon Tyne, U.K., in 2014.

From 2011 to 2014, he was a Part-Time Lecturer with the Faculty of Engineering and Environment, Northumbria University. Since 2014, he has been a Post-Doctoral Associate with the Center for Metamaterials and Integrated Plasmonics, Department of Electrical and Computer Engineering, Duke University. He authored or co-authored over 50 papers published in peer-reviewed international journals and conference proceedings. His research interests include antennas and propagation, antenna measurement techniques, microwave and millimeter-wave imaging, frequency-diverse imaging, metamaterials, and wireless power transfer.

Dr. Yurduseven received a best paper award at the Mediterranean Microwave Symposium in 2012. He also received the Academic Excellence Award from the Association of British–Turkish Academics, London, in 2013. He is a member of the European Association on Antennas and Propagation. He serves as a Reviewer for the IEEE Transactions on Antennas and Propagation, the IEEE Transactions on Microwave Theory and Techniques, and the IEEE Antennas and Wireless Propagation Letters.

JONAH N. GOLLUB (M'16) received the B.A. degree in physics from Reed College in 2000, and the Ph.D. degree in physics from the University of California, San Diego, in 2009. His thesis was on characterizing the hybridization of metamaterials with magnetic materials. From 2010 to 2012, he was a Lead Modeling and Simulation Scientist with a startup company developing surface metamaterials with applications targeted toward imaging and biological detection under DARPA, MDA, Army, and NSF funded efforts. He joined Duke University as a Research Scientist in 2013 and is currently focused on developing real-time millimeter wave imaging approaches, which utilize frequency diverse antennas and compressive imaging techniques.

ALEC ROSE received the B.S. degree in physics from Boston College in 2009, and the Ph.D. degree in electrical and computer engineering from Duke University in 2013, under the supervision of Prof. D. R. Smith. His Ph.D. thesis was on theory and design of nonlinear metamaterials.

As a member of the Smith Research Group, he made contributions to the fields of nonlinear electromagnetic metamaterials and plasmonics. He has become the Director of Advanced Development with Evolv Technologies, Inc., Waltham, MA, a startup company, where he has involved in advancing millimeter-wave sensing systems for physical security applications.

Dr. Rose received the Outstanding ECE Ph.D. Dissertation Award from Duke University for his Ph.D. thesis in 2013.

DANIEL L. MARKS was born in Chicago, Illinois, in 1973. He received the B.S., M.S., and Ph.D. degrees from the University of Illinois, Urbana–Champaign, in 1995, 1998, and 2001, respectively. From 2001 to 2008, he was a Research Scientist with the Biophotonics Laboratory, University of Illinois, Urbana–Champaign. He has been an Associate Research Professor with the Department of Electrical and Computer Engineering, Duke University, since 2009. He has authored 85 research articles. He holds 17 patents. His research interests include optics, optical design, computational imaging, millimeter-wave and terahertz imaging, metamaterials, and synthetic electromagnetic structures. He has been an Editor of the *Applied Optics*.

DAVID R. SMITH (M'98) received the Ph.D. degree in physics from the University of California at San Diego (UCSD), in 1994. He is currently the Department Chair and the James B. Duke Professor of Electrical and Computer Engineering with Duke University and the Director of the Center for Metamaterials and Integrated Plasmonics. He is an Adjunct Professor with the Physics Department, University of California at San Diego, Affiliate Faculty with the Electrical and Computer Engineering Department, University of Washington, and a Visiting Professor of Physics with Imperial College, London. His research interests include the theory, simulation, and characterization of unique electromagnetic structures, including photonic crystals and metamaterials, and the applications of such materials.

While at UCSD, he and his colleagues demonstrated the first left-handed (or negative index) metamaterial at microwave frequencies in 2000. He has authored over 200 publications on matematerials and plasmonics, and was selected by ISI-Reuters as a Citation Laureate in 2009 for the most number of highly cited papers in physics over the last decade. He was once again recognized as one of the Highly Cited Researches 2014 by ISI-Reuters in the category of physics.

In 2002, he was elected as a member of The Electromagnetics Academy. In 2005, he was part of a five-member team that received the Descartes Research Prize by the European Union for their contributions to metamaterials and other novel electromagnetic materials. He also received the Stansell Research Award from the Pratt School of Engineering, Duke University, in 2005. In 2006, he was selected as one of the Scientific American 50, a group recognized by the editors of Scientific American for achievements in science, technology, and policy. His work has twice appeared on the cover of *Physics Today*, and twice has been selected as one of the Top Ten Breakthroughs of the year by *Science Magazine*. In 2013, he was a co-recipient of the James C. McGroddy Prize for New Materials by the American Physical Society.

In 2006, he, along with colleague Prof. J. Pendry, suggested metamaterials could be used to design an electromagnetic cloak, introducing the new design tool of transformation optics. In 2013, he was asked to write an op-ed piece for the *New York Times* on cloaking research.

Dr. Smith served as the Founding and the Acting Director of the Metamaterials Commercialization Center, a unit within the Intellectual Ventures, Bellevue, WA, in 2013, dedicated to commercializing metamaterials concepts. MCC has thus far produced three spin out companies: Kymeta Corporation, Redmond, WA, Evolv Technologies, Waltham, MA, and Echodyne, Bellevue, WA. He serves on the Advisory Board for Kymeta, which targets metamaterial-based antennas for satellite communications. He is a Co-Founder of Evolv Technologies, which targets metamaterial apertures for security screening applications, and Echodyne, which is seeking to apply metamaterial apertures to radar applications.

• • •